Journal of Materials Chemistry A

ROYAL SOCIETY OF CHEMISTRY

PAPER

View Article Online
View Journal | View Issue

Cite this: J. Mater. Chem. A, 2020, 8, 1749

3D printing-based cellular microelectrodes for high-performance asymmetric quasi-solid-state micro-pseudocapacitors†

Teng Wang,‡[ab] Xiaocong Tian, ‡*[a] Liang Li,[b] Luhua Lu, [a] Shuen Hou,[a] Guozhong Cao *[c] and Hongyun Jin *[a]

Micro-supercapacitor is a member of the miniaturized energy storage device family, which offers great advantages on power density and life span. However, the limited device capacitance and narrow voltage window limit its energy density, hindering its application. In the present work, a novel micro-pseudocapacitor (MPC) constructed *via* the facile extrusion-based 3D printing technique has been demonstrated to deliver efficient charge storage with high device capacitance and moderate voltage window. Such an asymmetric MPC is constructed with 3D-printing-enabled asymmetric interdigitated cellular microelectrodes; in which, one is Ni–Co–O nanosheets grown on macroporous 3D reduced GO (3DG) microelectrode and the other is MnO_2 nanosheets grown on 3DG. Such an MPC offers facilitated fast electron transport, ionic diffusion, large number of active sites and desired porosity for electrolyte penetration. The asymmetric MPC shows a high specific capacity of 500 mC cm^{-2}, an energy density of 90 μW h cm^{-2} and a voltage window of 1.3 V. A device cycling stability with 10 000 charge and discharge cycles is also achieved for the as-fabricated asymmetric MPCs. These encouraging results may open a new avenue to design and fabricate state-of-the-art miniaturized electrochemical energy storage devices with customized geometries.

Received 16th October 2019
Accepted 11th December 2019

DOI: 10.1039/c9ta11386j

rsc.li/materials-a

1. Introduction

Miniaturized and portable electronic devices are essential in the daily life of today's modern society. Micro-sized planar electrochemical energy storage devices (PEESDs) offer an ideal option as energy suppliers[1–4] for such devices. Typical PEESDs, including micro-batteries and micro-supercapacitors (MSCs), have drawn great interests in this field due to their prospective electrochemical performances.[5,6] Among these, MSCs belong to a promising PEESD with desirable power density and long cycling stability.[7–9] However, a critical factor hindering its further development is the unsatisfactory specific energy density (low capacity and working voltage) due to the surface or near-surface mechanisms.[10,11] Towards this end, MSCs constructed with superior electrochemical performances, especially high areal capacitance and moderate device voltage window, are urgently needed for future applications.

According to the intrinsic capacitive charge storage mechanism, MSC electrodes are classified as electric double-layer micro-capacitor (EDL-MC) electrodes[12–14] and micro-pseudocapacitor (MPC) electrodes.[15–17] Among them, the former one stores energy through a simple EDL formation at the electrolyte–electrode interfaces and commonly uses carbon based materials.[18] Apart from EDL-MC electrodes, metal oxides, metal sulfides and conductive polymers are commonly used as electrodes in MPCs, and offer high capacities (capacitances) and energy density due to the occurrence of faradaic redox reactions.[19] For both EDL-MC and MPC electrodes, their assembly into an integrated two-electrode system is essential to realize a full EDL-MC or MPC device delivering capacitance values and operational voltage window.[20] In this regard, MSC configuration, namely symmetric or asymmetric type, will greatly affect the device energy storage performance. For symmetric MSCs, the device voltage of MSCs is limited with the presence of water splitting. To circumvent such limitations and enhance the energy storage performance, the construction of asymmetric MSCs with three-dimensional (3D) architectures and customized configurations is one of the promising approaches.

As of today, most MSC fabrication processes are based on lithography, in which a number of high-cost fabrication

[a]Engineering Research Center of Nano-Geo Materials of Ministry of Education, Faculty of Materials Science and Chemistry, China University of Geosciences, Wuhan 430074, China. E-mail: tianxc@cug.edu.cn; jinhongyun@cug.edu.cn

[b]Key Laboratory for Green Chemical Process of Ministry of Education, Hubei Key Laboratory of Plasma Chemistry and Advanced Materials, School of Materials Science and Engineering, Wuhan Institute of Technology, Wuhan 430205, China

[c]Department of Materials Science and Engineering, University of Washington, Seattle, WA, 98195-2120, USA. E-mail: gzcao@u.washington.edu

† Electronic Supplementary Information (ESI) available: See DOI: 10.1039/x0xx00000x

‡ These authors contributed equally to this work.

techniques are required to enable the patterning of current collectors or microelectrodes.[21–23] Afterwards electrode growth in symmetric and asymmetric configurations is conducted to complete the fabrication of full devices. In comparison, 3D printing is recognized as a powerful approach for MSC construction with customized geometries.[24–26] Among various 3D printing techniques, extrusion-based 3D printing offers huge advantages in a ready operation with controlled chemical components.[27–29] This extrusion printing technique is quite favorable for the fabrication of asymmetric thick microelectrodes due to the direct microelectrode patterning as well as unique electrode tuning.[30,31] Graphene oxide (GO) based printing has been recently developed with great promises in the fabrication of efficient energy storage devices.[32–35] However, these devices are mostly employed in EDL-MCs and thus are limited by the low electrode (and even device) capacitance. To address this concern, reduced GO (rGO) boosted MPCs with a desired device configuration (such as asymmetric type) need to be designed and printed urgently.

In this work, the MPC constructed *via* a facile extrusion-based 3D printing technique is demonstrated to achieve efficient energy storage with high capacitance and moderate voltage window. Such an MPC is composed of the asymmetric interdigitated thick cellular microelectrodes, in which one is Ni–Co–O nanosheets grown on macroporous 3D rGO microelectrode (denoted as NC-3DG) and the other is MnO_2 nanosheets grown on 3DG microelectrode (denoted as M-3DG). To obtain this desired MPC, interdigitated macroporous 3D rGO (3DG) is firstly extruded from a well-engineered printable GO ink and it acts as the patterned conductive 3D cellular framework with controlled thicknesses. Subsequently, metal oxide growth is conducted to realize the asymmetric pseudocapacitive metal oxide based MPCs, which offer facilitated electron transport, ionic diffusion channel, large active sites and desired porosity for electrolyte penetration. The 3D-printing enabled full asymmetric MPC shows a moderate voltage window of 1.3 V and delivers a high device specific capacity of 500 mC cm^{-2} and a device energy density of 90 μW h cm^{-2}, which are superior to most of the previously reported MPC devices. A robust device cycling stability during 10 000 charge and discharge cycles is also achieved for the as-fabricated MPCs. As a result, this work may open up a wide range of opportunities for the design and construction of state-of-the-art miniaturized electrochemical energy storage devices.

2. Experimental section

2.1 3D printing

A 1 wt% aqueous GO dispersion was purchased from Shanghai Ashine and used directly without further purification. To obtain 3D printable GO ink with suitable rheology behaviors, the GO dispersion was stirred with a continuous heating at 130 °C to evaporate the excess water. After the loading of the obtained GO ink into a syringe with a 23-gauge nozzle, the GO 3D interdigitated structure was pneumatically printed (0.1–0.2 MPa) using a 3D extrusion system with a designed programmer. As-printed GO 3D framework was then freeze-dried and further reduced at an optimized annealing temperature of 700 °C under Ar/H_2 gas for 6 h to obtain the interdigitated 3DG microelectrodes.

For comparison, the 3D printing of interdigitated packed graphene (PG) microelectrode was also employed where the ink was prepared by directly mixing 400 mg of rGO powder and 100 mg of poly (vinylidene fluoride) in 1.5 mL *N*-methyl pyrrolidone using a mortar and pestle. After its printing, it was soaked in DI water for 8 h, followed by freeze drying to obtain the interdigitated PG microelectrodes.

2.2 Asymmetric MPC fabrication

The growth of pseudocapacitive metal oxide was conducted using a two-step process. The first step was the growth of Ni–Co–O nanosheets on one side of the interdigitated 3D rGO framework microelectrode. At first, the electrodeposition of Ni–Co–O precursors was conducted in a three-electrode configuration by using the HgO/Hg and Pt plate as the reference electrode and counter electrode, respectively. Before the electrodeposition process, 3D rGO framework in the electrodeposition electrolyte was soaked for 30 min in order to improve the inner rGO wetting. To obtain the electrodeposition electrolyte with various Ni/Co mole ratios, 2.91 g of $Ni(NO_3)_2 \cdot 6H_2O$ was dissolved in 10 mL deionized water, followed by mixing with 1.46 g, 2.90 g and 14.60 g $Co(NO_3)_2 \cdot 6H_2O$. Later, the corresponding Ni–Co–O precursors were electrodeposited potentiostatically at −1 V for 400 s. An annealing treatment at 300 °C was then employed for 2 h in air to obtain the NC-3DG microelectrodes with corresponding different Ni/Co mole ratios.

The subsequent MnO_2 growth on the other side of interdigitated 3DG microelectrodes was the second step of the process. Specifically, the electrodeposition electrolyte was prepared by mixing with 25 mM $Mn(NO_3)_2$ and 25 mM $NaNO_3$ aqueous solution.[36] The electrodeposition was conducted potentiostatically at 1 V for 1000 s in a three-electrode configuration. The process was identical to that of the Ni–Co–O precursor electrodeposition process.

In the control experiment for the fabrication of asymmetric PG-based MPCs, the growth of NC-based pseudocapacitive materials was conducted using the same procedure as described above. For the subsequent MnO_2 growth, the electrodeposition parameters were the same while the post annealing treatment temperature was 300 °C.

2.3 Characterization

The rheological behaviors of the GO ink were determined using an Anton Paar 302 rheometer at 25 °C. The shear stress–modulus curves of ink were obtained at a stable angular frequency of 6.28 rad s^{-1}. The phases of as-deposited pseudocapacitive metal oxides were observed using the X-ray diffraction (XRD) technique on a D8 Discover X-ray diffractometer. Simulated PXRD patterns were obtained using the FullProf program. Scanning electron microscopy (SEM) images and accompanying energy dispersive spectrometry (EDS) data were collected on a JEOL-7100F field-emission scanning electron microscope. Raman spectra were recorded on a Renishaw RM-1000 laser Raman microscopy system. Transmission electron

microscopy (TEM) images, selected area electron diffraction (SAED) patterns, and EDS spectra conducted with a beryllium window were recorded on a CM12/STEM microscope at an acceleration voltage of 120 kV. X-Ray photoelectron spectroscopy (XPS) spectra were collected on an ESCALAB 250Xi instrument. The electrochemical performances of fabricated MPCs were measured using cyclic voltammetry (CV), galvanostatic charge–discharge (GCD) and electrochemical impedance spectroscopy (EIS) methods with a two-electrode configuration in the KOH/PVA gel electrolyte. All electrochemical tests were performed on a CHI760E electrochemical workstation at ambient temperature.

3. Results and discussion

Fig. 1 displays an overview of the fabrication process of the 3D-printed asymmetric NC-3DG//M-3DG MPCs. The 3DG framework was firstly printed in the interdigitated pattern and with a desired thick microelectrode using an extrusion 3D printing, where an additive-free highly concentrated GO aqueous suspension was employed as the printable ink. To obtain such an ink, a well-dispersed aqueous suspension containing 10 mg mL^{-1} of GO was evaporated to a much high concentrated suspension ($\approx$120 mg mL^{-1}) with a continuous heating at 130 °C.[35] As seen from Fig. 2a, once the ink extruded from the syringe needle, a continuous filament was observed without the occurrence of the ink falling or blocking, implying the good printable properties. The measured ink rheological data were collected as shown in Fig. S1,† where the shear-thinning and non-Newtonian fluid behaviors of GO ink were demonstrated, further confirming its suitable 3D printable properties. After the printing of GO interdigitated 3D framework, a high-temperature post treatment in Ar/H_2 was subsequently conducted to obtain the corresponding interdigitated 3DG microelectrode, as shown in the inset optical image of Fig. 2a. In such a framework structure, the open cellular interconnected network was observed with abundant macroscale pore spaces (Fig. S2a†). In contrast, no cellular structure was found for the interdigitated PG as shown in Fig. S2b.†

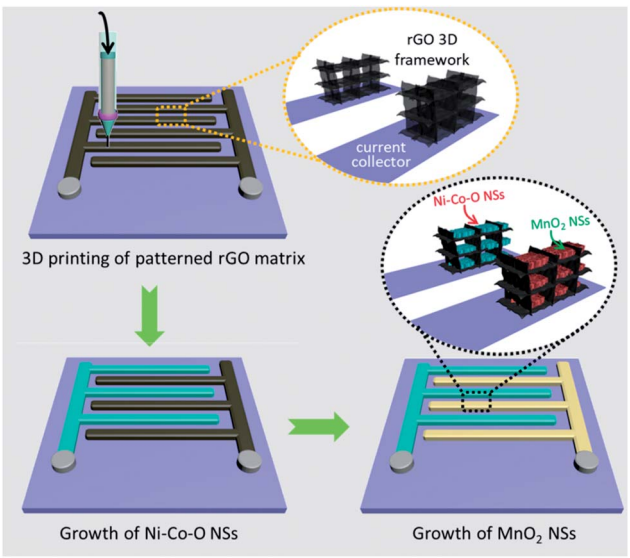

Fig. 1 Schematic of the process for the fabrication of asymmetric NC-3DG//M-3DG MPCs.

Pseudocapacitive materials are well-known as high-capacitance electrode components. To further boost the MPC electrochemical performance, the sheet surfaces of the two 3D-printed macroporous rGO interdigitated microelectrodes were modified. As illustrated in Fig. 1, the sequential growth of Ni–Co–O and MnO_2 nanosheets was carried out separately on the two interdigitated cellular microelectrodes. Such growth was based on the abundant macroporous spaces and good wetting property of the rGO framework. The obvious color distinction in the inset of Fig. 2b implies the successful realization of the asymmetric construction of micro-sized M-3DG and NC-3DG interdigitated microelectrodes. XRD patterns, simulated PXRD patterns (Fig. S3) and Raman spectra (Fig. S4†) further verified the formation of M-3DG and NC-3DG phases. Typical SEM images and TEM image of these microelectrodes are displayed in Fig. 2c–f. The microelectrode extrusion followed the layer-by-layer printing process; the resulting layered structure of the extruded cellular microelectrodes was readily observed as shown in Fig. 2c. An approximate 350 μm thickness of each layer was measured, which was slightly larger than that of the syringe diameter. It was also observed that the continuous macroscale pores in the 3D rGO framework were retained, permitting faster ionic diffusion. Moreover, as seen from Fig. 2d, the as-grown nanosheet components were uniformly attached on the rGO sheet, suggesting the conformal growth as well as the high microelectrode volumetric/areal ratio. The corresponding EDS quantitative analysis results showed that the Ni/Co mole ratio was 1 : 2 for NC-3DG cellular microelectrodes (inset of Fig. 2e). As shown in Fig. 2e, f and S5,† the well-grown Ni–Co–O and MnO_2 nanosheets were clearly observed, demonstrating a further enhanced surface contact area between microelectrodes and the electrolyte. The elemental composition and valence states of NC-3DG and M-3DG were established by XPS results (Fig. S6 and S7†), confirming the successful deposition and good attachment of Ni–Co–O and MnO_2 nanosheets on the cellular 3DG interconnected network.[37,38]

3DG frameworks are well-known as promising electrodes for electrochemical capacitive energy storage with high electrical conductivity and desired porous microstructure.[39,40] Hence, in this work, such microstructures were directly achieved in an interdigitated pattern using a graphene oxide 3D printing method and post treatment. The post annealing treatment temperature for the 3DG framework was set at 700 °C with the optimized electrochemical behavior as shown in CV curves (Fig. S8†). Then, with a further introduction of optimized higher-capacitance pseudocapacitive components with the maintained 3D porous framework microstructure, remarkable electrochemical redox reactions accompanying the facilitated electron and ionic diffusion kinetics were expected. Moreover, the pseudocapacitive components of MnO_2 and Ni–Co–O nanosheets were grown on each side of the interdigitated cellular microelectrodes and resulted in a wider device operating voltage window of up to 1.3 V (Fig. 3a). This enhancement

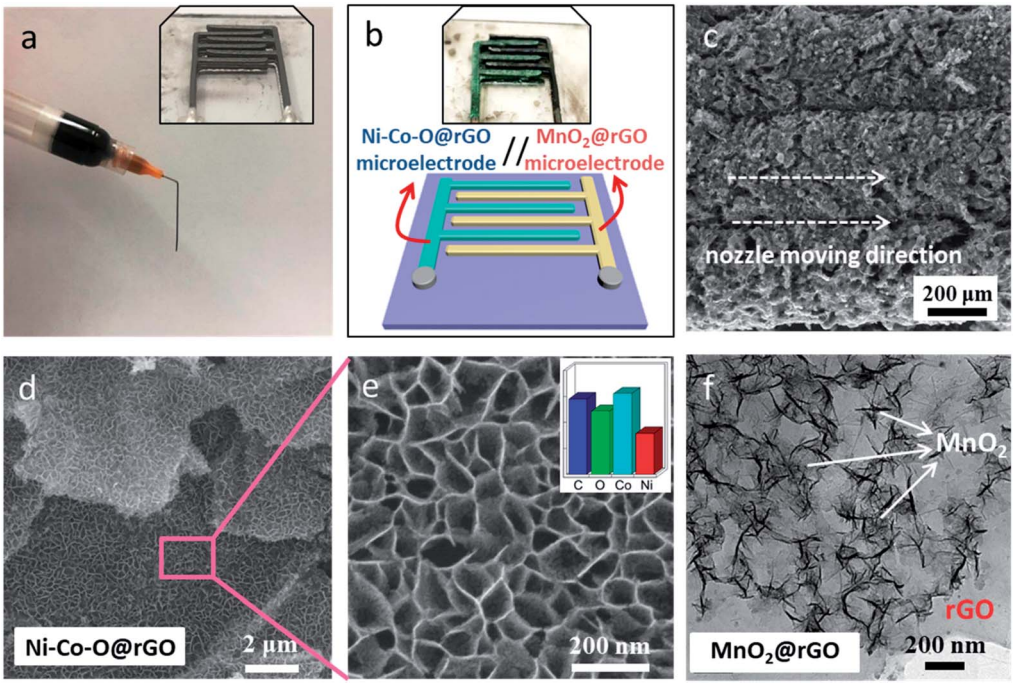

Fig. 2 (a) Optical images of an extrusion state of the GO ink from a syringe. The inset optical image is the corresponding patterned 3DG. (b) Schematic and corresponding optical image (inset) of the asymmetric NC-3DG//M-3DG MPCs. (c) A cross-sectional SEM image and (d and e) SEM images of NC-3DG microelectrodes with a Ni/Co mole ratio of 1 : 2. (f) A TEM image of M-3DG microelectrodes.

may be attributed to the reversible nature of the grown pseudocapacitive components of different suitable potential windows. To be more specific, the MnO_2 and Ni–Co–O nanosheets possess stable potential windows at 0–0.5 V and −0.8–0 V, respectively, as evaluated in a three-electrode configuration with Pt foil and Hg/HgO as the counter electrode and reference electrode, respectively, in the same alkaline electrolyte (Fig. S9†). According to the eqn (S1),† the achieved specific

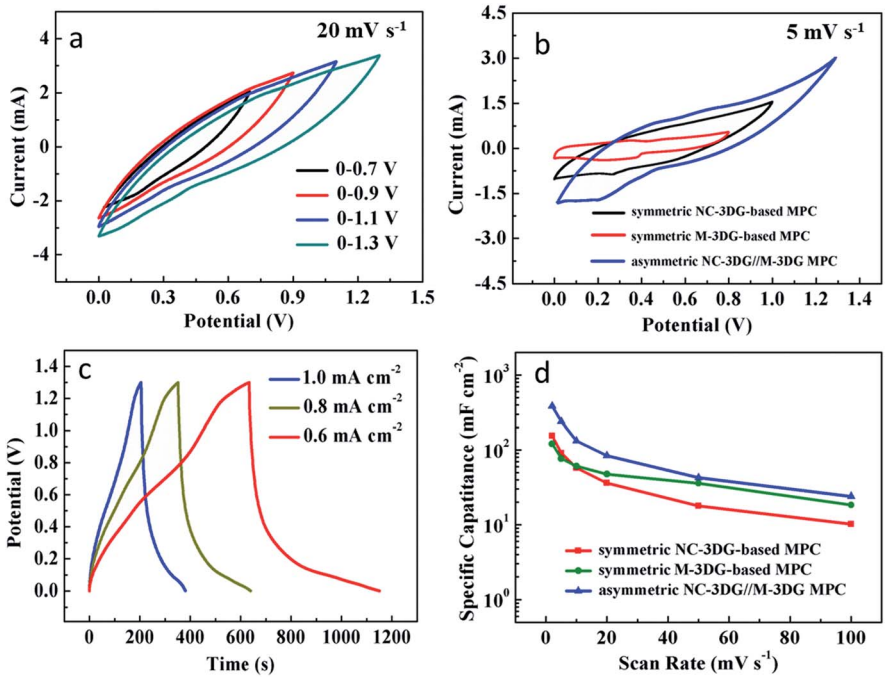

Fig. 3 (a and b) CV curves of (a) asymmetric NC-3DG//M-3DG MPCs (Ni/Co mole ratio is 1 : 2) and (b) its comparison with symmetric NC-3DG-based and M-3DG-based MPCs at different voltage windows. (c) GCD curves of asymmetric NC-3DG//M-3DG MPCs (Ni/Co mole ratio is 1 : 2) at 0–1.3 V. (d) Specific device capacitance values of asymmetric NC-3DG//M-3DG MPCs, symmetric NC-3DG-based and M-3DG-based MPCs.

capacitance values of MnO_2 and Ni–Co–O microelectrodes were thus calculated to be 69 and 327 mF cm^{-2}, respectively, at a scan rate of 5 mV s^{-1}, indicating a great promise for both of the electrode materials.

Based on the electrochemical results obtained in a three-electrode configuration, MnO_2 and Ni–Co–O microelectrodes are able to work as cathode and anode, respectively, when assembled to form an MPC. This assembly in a high integration degree was directly realized *via* 3D printing and electrodeposition in this work. The full-device electrochemical performances of integrated symmetric MPCs and asymmetric MPCs were evaluated in a two-electrode system as show in Fig. 3b–d. It is worth noting that the CV test result (Fig. S10†) indicated negligible capacity compared with that of the asymmetric NC-3DG//M-3DG MPC. For the asymmetric MPC, some small redox peaks were observed in the CV curves, which were consistent with the GCD curves (Fig. 3b and c). With a desired charge and discharge CV curves, the operating voltage window was set as 1.3 V, which was broader than those set for most of the reported MSCs, such as multi-walled CNT/V_2O_5 (0–0.8 V) and Si/TiC/carbon (−0.6–0.2 V) MSCs, as well as recently reported 3D-printed carbon nanotube-based MSCs.[11,41,42] The results indicated that electrochemical advantages of both MnO_2 and Ni–Co–O microelectrodes are employed at a high degree. Moreover, with a further comparison with symmetric NC-3DG-based and M-3DG-based MPCs, the charge and discharge current values of asymmetric NC-3DG//M-3DG MPCs exceed much along with a wider voltage window of 0.5 V (Fig. 3b). Based on eqn (S1) and (S2),† the specific device areal capacitance values of asymmetric NC-3DG//M-3DG MPCs (Ni/Co mole ratio = 1 : 2) reach 384 mF cm^{-2} (corresponding to a device capacity of 500 mC cm^{-2}) at a scan rate of 2 mV s^{-1}, while the 154 and 121 mF cm^{-2} (corresponding to the device capacity of 154 mC cm^{-2} and 97 mC cm^{-2}, respectively) were calculated for symmetric NC-3DG-based and M-3DG-based MPCs, respectively. A corresponding high device energy density of 90 μW h cm^{-2} was thus achieved for asymmetric MPCs according to eqn (S3).† Moreover, the realized high device capacity was much higher than those reported for many 3D-printed MSCs such as 3D-printing-stamped $Ti_3C_2T_x$ MSCs (37 mC cm^{-2}),[24] 3D-printed rGO MSCs (74 mC cm^{-2}),[43] 3D-printed GO/polyaniline (PANI)-based symmetric MSCs (123 mC cm^{-2})[44] and 3D-printed VO_x/rGO//graphene-vanadium nitride quantum dots (G–VNQDs)/rGO asymmetric MSC (333 mC cm^{-2}),[45] as displayed in Table S1,† further demonstrating the unique and advantageous 3DG design for MSCs.

It is well-known that the charge storage behaviors of pseudocapacitive nanomaterial electrodes are mainly based on adsorption/desorption and reversible redox reactions.[46] In this work, MnO_2 nanostructures depended on its reversible reaction ability with cations K^+, while Ni–Co–O nanomaterials possibly performed reversible reactions between Co and Ni transition species and OH^- anions, leading to a higher electrode capacitance value compared to that obtained for EDLC materials.[35,47] The presence of these pseudocapacitive components boosted the overall device capacitance with a suitable voltage setting as measured above. With a precise arrangement of the two sides of the interdigitated cellular microelectrodes, the ion diffusion pathway was also much shortened, further leading to a largely improved electrochemical kinetics. From the device capacitance evolution of as-fabricated three types of MPCs at various scan rates as displayed in Fig. 3d, it was observed that the symmetric M-3DG-based MPCs exhibited lower device capacitance at low scan rates but possessed better rate capability with higher capacitance at high scan rates compared with symmetric NC-3DG-based MPC (Ni/Co mole ratio was 1 : 2). In contrast, asymmetric NC-3DG//M-3DG MPCs offered higher device capacitance values at both low and high scan rates, further revealing their superior advantages in the efficient electrochemical energy.

To further confirm the critical role of 3D-printed 3DG microstructures in as-fabricated asymmetric MPCs, a control experiment of asymmetric PG-based MPC construction was also employed. As shown in Fig. 4a, the discharging current values of asymmetric 3DG-based MPCs were much greater than those of the asymmetric PG-based one, indicating the charge storage and capacitance enhancement. At the scan rate of 2 mV s^{-1}, the calculated device capacitance of asymmetric 3DG-based MPC was more than 2.5-fold higher than that of the asymmetric PG-based device, as displayed in Fig. 4b. The corresponding device capacitance values calculated at various scan rates also confirmed such a charge storage enhancement in the presence of 3DG. It was believed that the charge storage behaviors were largely dependent on the microstructure of the as-fabricated MPCs. Specifically, for asymmetric 3DG-based MPCs, the 3DG aspect enabled not only the external, but also the internal sites of pseudocapacitive metal oxide materials, while the pseudocapacitive material growth only took place on external sites of the PG-based device. Correspondingly, the specific amount of pseudocapacitive materials in asymmetric 3DG-based MPCs was much more than that in the asymmetric PG-based MPCs (Fig. 4c and d). Thus, although the electrical transport between the pseudocapacitive materials and current collectors were enhanced with the presence of PG, the amount of electrolyte ions were still insufficient. In comparison, the 3D continuous electrical transport and ionic diffusion was also realized, resulting in the fast electrical transport as well as the presence of sufficient amount of diffused electrolyte ions.

In order to create a deeper understanding of the device structure-electrochemical performance relationship, a range of MPCs with tunable Ni–Co–O microstructures were fabricated. With different Ni/Co mole ratios (1 : 0.5, 1 : 2 and 1 : 5) in electrodeposited electrolyte solutions, corresponding various Ni–Co–O microelectrodes were obtained as Ni–Co–O(0.5), Ni–Co–O(2) and Ni–Co–O(5), respectively, grown on the 3D rGO framework. They are further denoted as NC-3DG(0.5), NC-3DG(2) and NC-3DG(5), and their morphologies are displayed in Fig. S11.† At a mole ratio of 1 : 0.5, the growth of Ni–Co–O nanosheets is less flourishing compared with that of the NC-3DG(2) one. The corresponding EDS data further illustrates the evolution of various elemental content ratios for the obtained NC-3DG cellular microelectrodes. With increasing Co ratios, substantial increment of Ni and Co contents is observed compared with the C content, suggesting a promotional effect

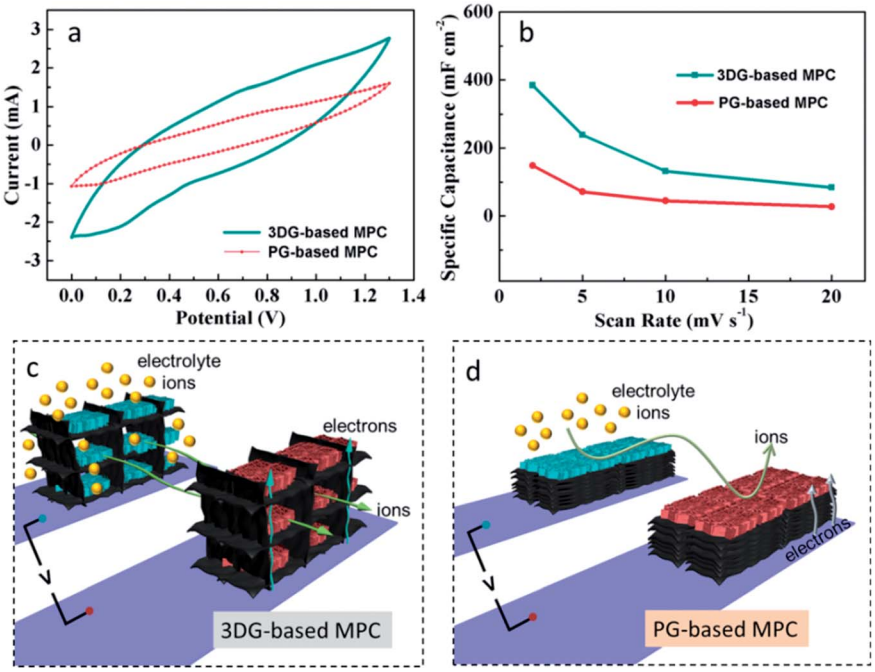

Fig. 4 (a) CV curves at a scan rate of 10 mV s^{-1} and (b) corresponding specific capacitances of 3DG-based and PG-based asymmetric MPCs. (c and d) Schematic explaining the charge storage mechanisms of (c) 3DG-based and (d) PG-based asymmetric MPCs.

on the grown amount. Moreover, mole ratios of the grown Ni/Co are in accordance with those of the electrolyte Ni/Co ion contents.

With a further increase in the Co amount to 1 : 5, the overgrown Ni–Co–O nanowires cover the top of nanosheets, indicating the blocked ion diffusion pathway of NC-3DG(5).

With tunable Ni–Co–O depositional electrolyte contents, NC-3DG based cellular microelectrodes were finely controlled with achieved NC-3DG(0.5), NC-3DG(2) and NC-3DG(5) based asymmetric MPCs. As shown in Fig. 5a and b, the electrochemical discharge behavior is slightly different, leading to the different resultant device capacitance values (eqn (S4)†). It can be seen

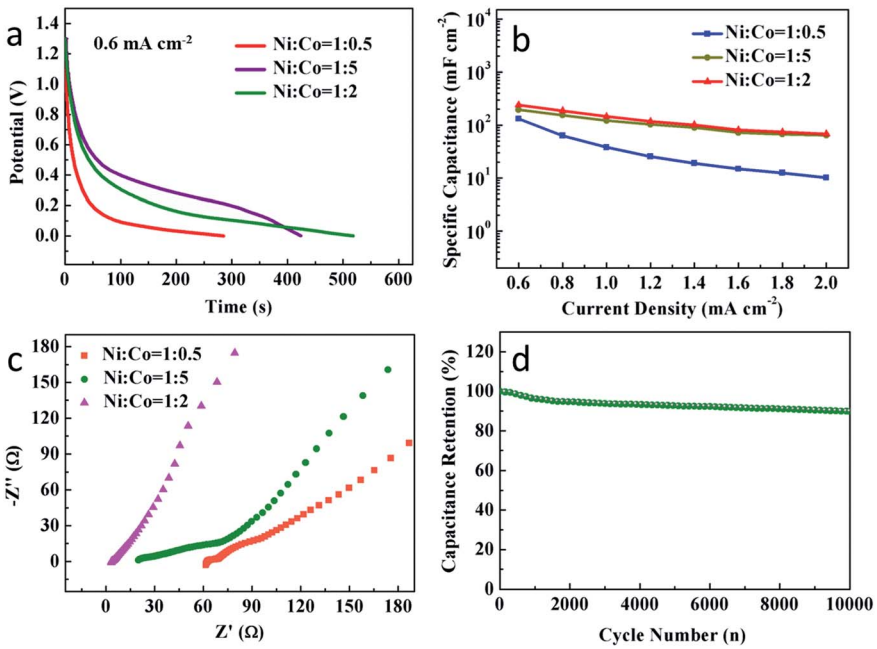

Fig. 5 (a) GCD discharge curves, (b) corresponding capacitance values and (c) Nyquist plots of NC-3DG(0.5), NC-3DG(2) and NC-3DG(5) matched with M-3DG MPCs. (d) Cycling stability of NC-3DG(2)//M-3DG asymmetric MPCs.

that asymmetric NC-3DG(2)//M-3DG MPCs deliver slightly higher capacitance compared with that of NC-3DG(5)//M-3DG MPCs, and even much higher than that of NC-3DG(0.5)//M-3DG at various current densities. The differences in delivered electrochemical performances are a result of different morphologies and elemental contents of the as-grown NC-3DG microelectrodes, which may affect the electrical transport and ionic diffusion significantly.

EIS is an efficient method to acquire the information on the electrical and ionic transport of materials and devices.[48] The obtained Nyquist plots from the EIS test showed that the smallest high-frequency intercept value with the real axis was observed for NC-3DG(2)//M-3DG MPCs among all the as-fabricated MPCs, revealing the corresponding lowest equivalent series resistance (ESR) of 3.5 Ω (Fig. 5c).[49] The above results explain the slight differences existing in the as-fabricated various asymmetric 3DG MPCs. After 10 000 ultra-long charge and discharge cycles, the remarkable device capacitance retention was achieved at 89.9% for NC-3DG(2)//M-3DG MPCs (Fig. 5d), further demonstrating the great advantages of such optimized microelectrode structures along with the asymmetric configuration design.

4. Conclusion

Asymmetric NC-3DG//M-3DG MPCs were fabricated *via* a simple direct graphene oxide ink writing process, and their efficient energy storage behaviors of high device areal capacity and moderate voltage window were demonstrated in this work. The unique design of the 3DG supporter offers great advantages for the facilitated electrical transport, ionic diffusion channel, large active sites and rational pore engineering. With these desired characteristics, the resultant asymmetric NC-3DG(2)//M-3DG MPCs delivered superior electrochemical performances with high specific capacity of up to 500 mC cm^{-2} (a corresponding high device capacitance of 384.9 mF cm^{-2} and a high device energy density of 90 μW h cm^{-2}), and a moderate voltage window of 1.3 V. A robust device cycling stability during 10 000 charge and discharge cycles was also achieved for the fabricated MPCs. The developed MPC construction strategy opens a new avenue to design and manufacture state-of-the-art miniaturized electrochemical energy storage devices.

Conflicts of interest

There are no conflicts of interest to declare.

Acknowledgements

This work was supported by the National Natural Science Foundation of China (51802292), the Nation Science Foundation (CBET-1803256), the Fundamental Research Funds for the Central Universities (CUG170690), the Hubei Science and Technology Innovation Project (2018AAA015, 2017AAA112), the Research Funds for Engineering Research Center of Nano-Geo Materials of Ministry of Education (NGM2019KF015).

Notes and references

1 N. A. Kyeremateng, T. Brousse and D. Pech, *Nat. Nanotechnol.*, 2016, **12**, 7.
2 W. Lv, Z. Li, Y. Deng, Q.-H. Yang and F. Kang, *Energy Storage Mater.*, 2016, **2**, 107–138.
3 Y. Zhong, X. Xia, W. Mai, J. Tu and H. J. Fan, *Adv. Mater. Technol.*, 2017, **2**, 1700182.
4 X. Cai, C. Zhang, S. Zhang, Y. Fang and D. Zou, *J. Mater. Chem. A*, 2017, **5**, 2444–2459.
5 S.-W. Kim, K.-N. Kang, J.-W. Min and J.-H. Jang, *Nano Energy*, 2018, **50**, 410–416.
6 A. Lamberti, N. Garino, A. Sacco, S. Bianco, A. Chiodoni and C. Gerbaldi, *Electrochim. Acta*, 2015, **151**, 222–229.
7 H. Xiao, Z.-S. Wu, L. Chen, F. Zhou, S. Zheng, W. Ren, H.-M. Cheng and X. Bao, *ACS Nano*, 2017, **11**, 7284–7292.
8 B. Song, L. Li, Z. Lin, Z.-K. Wu, K.-s. Moon and C.-P. Wong, *Nano Energy*, 2015, **16**, 470–478.
9 Z.-S. Wu, Y.-Z. Tan, S. Zheng, S. Wang, K. Parvez, J. Qin, X. Shi, C. Sun, X. Bao, X. Feng and K. Müllen, *J. Am. Chem. Soc.*, 2017, **139**, 4506–4512.
10 C. Lethien, J. Le Bideau and T. Brousse, *Energy Environ. Sci.*, 2019, **12**, 96–115.
11 P. Huang, C. Lethien, S. Pinaud, K. Brousse, R. Laloo, V. Turq, M. Respaud, A. Demortière, B. Daffos, P. L. Taberna, B. Chaudret, Y. Gogotsi and P. Simon, *Science*, 2016, **351**, 691–695.
12 J. Chmiola, C. Largeot, P.-L. Taberna, P. Simon and Y. Gogotsi, *Science*, 2010, **328**, 480–483.
13 P. He, Z. Ding, X. Zhao, J. Liu, Q. Huang, J. Peng and L.-Z. Fan, *Carbon*, 2019, **155**, 453–461.
14 X. Ma, X. Hong, L. He, L. Xu, Y. Zhang, Z. Zhu, X. Pan, J. Zhu and L. Mai, *ACS Appl. Mater. Interfaces*, 2018, **11**, 948–956.
15 X. Tian, M. Shi, X. Xu, M. Yan, L. Xu, A. Minhas-Khan, C. Han, L. He and L. Mai, *Adv. Mater.*, 2015, **27**, 7476–7482.
16 P. Li, J. Li, Z. Zhao, Z. Fang, M. Yang, Z. Yuan, Y. Zhang, Q. Zhang, W. Hong and X. Chen, *Adv. Sci.*, 2017, **4**, 1700003.
17 C. Couly, M. Alhabeb, K. L. Van Aken, N. Kurra, L. Gomes, A. M. Navarro-Suárez, B. Anasori, H. N. Alshareef and Y. Gogotsi, *Adv. Electron. Mater.*, 2018, **4**, 1700339.
18 Z.-S. Wu, X. Feng and H.-M. Cheng, *Natl. Sci. Rev.*, 2013, **1**, 277–292.
19 Y. Shi, L. Peng, Y. Ding, Y. Zhao and G. Yu, *Chem. Soc. Rev.*, 2015, **44**, 6684–6696.
20 M. Beidaghi and Y. Gogotsi, *Energy Environ. Sci.*, 2014, **7**, 867.
21 H. Hu, Z. Pei and C. Ye, *Energy Storage Mater.*, 2015, **1**, 82–102.
22 R. Hou, G. S. Gund, K. Qi, P. Nakhanivej, H. Liu, F. Li, B. Y. Xia and H. S. Park, *Energy Storage Mater.*, 2019, **19**, 212–241.
23 S. Lochmann, J. Grothe, K. Eckhardt, D. Leistenschneider, L. Borchardt and S. Kaskel, *Nanoscale*, 2018, **10**, 10109–10115.
24 C. Zhang, M. P. Kremer, A. Seral-Ascaso, S.-H. Park, N. McEvoy, B. Anasori, Y. Gogotsi and V. Nicolosi, *Adv. Funct. Mater.*, 2018, **28**, 1705506.

25 K. Fu, Y. Wang, C. Yan, Y. Yao, Y. Chen, J. Dai, S. Lacey, Y. Wang, J. Wan, T. Li, Z. Wang, Y. Xu and L. Hu, *Adv. Mater.*, 2016, **28**, 2587–2594.
26 K. Sun, T.-S. Wei, B. Y. Ahn, J. Y. Seo, S. J. Dillon and J. A. Lewis, *Adv. Mater.*, 2013, **25**, 4539–4543.
27 C. Zhu, T. Y.-J. Han, E. B. Duoss, A. M. Golobic, J. D. Kuntz, C. M. Spadaccini and M. A. Worsley, *Nat. Commun.*, 2015, **6**, 6962.
28 Q. Zhang, F. Zhang, S. P. Medarametla, H. Li, C. Zhou and D. Lin, *Small*, 2016, **12**, 1702–1708.
29 E. García-Tuñon, S. Barg, J. Franco, R. Bell, S. Eslava, E. D'Elia, R. C. Maher, F. Guitian and E. Saiz, *Adv. Mater.*, 2015, **27**, 1688–1693.
30 X. Tian, J. Jin, S. Yuan, C. K. Chua, S. B. Tor and K. Zhou, *Adv. Energy Mater.*, 2017, **7**, 1700127.
31 L. Zhou, W. Ning, C. Wu, D. Zhang, W. Wei, J. Ma, C. Li and L. Chen, *Adv. Mater. Technol.*, 2019, **4**, 1800402.
32 V. G. Rocha, E. García-Tuñón, C. Botas, F. Markoulidis, E. Feilden, E. D'Elia, N. Ni, M. Shaffer and E. Saiz, *ACS Appl. Mater. Interfaces*, 2017, **9**, 37136–37145.
33 S. D. Lacey, D. J. Kirsch, Y. Li, J. T. Morgenstern, B. C. Zarket, Y. Yao, J. Dai, L. Q. Garcia, B. Liu, T. Gao, S. Xu, S. R. Raghavan, J. W. Connell, Y. Lin and L. Hu, *Adv. Mater.*, 2018, **30**, 1705651.
34 K. Fu, Y. Yao, J. Dai and L. Hu, *Adv. Mater.*, 2017, **29**, 1603486.
35 T. Wang, L. Li, X. Tian, H. Jin, K. Tang, S. Hou, H. Zhou and X. Yu, *Electrochim. Acta*, 2019, **319**, 245–252.
36 Z. Liu, X. Tian, X. Xu, L. He, M. Yan, C. Han, Y. Li, W. Yang and L. Mai, *Nano Res.*, 2017, **10**, 2471–2481.
37 H. Feng, S. Gao, J. Shi, L. Zhang, Z. Peng and S. J. E. A. Cao, *Electrochim. Acta*, 2019, **299**, 116–124.
38 S. Liu, Y. Zhu, J. Xie, Y. Huo, H. Y. Yang, T. Zhu, G. Cao, X. Zhao and S. J. A. E. M. Zhang, *Adv. Energy Mater.*, 2014, **4**, 1301960.
39 B. G. Choi, M. Yang, W. H. Hong, J. W. Choi and Y. S. Huh, *ACS Nano*, 2012, **6**, 4020–4028.
40 Z.-S. Wu, Y. Sun, Y.-Z. Tan, S. Yang, X. Feng and K. Müllen, *J. Am. Chem. Soc.*, 2012, **134**, 19532–19535.
41 D. Kim, J. Yun, G. Lee and J. S. Ha, *Nanoscale*, 2014, **6**, 12034–12041.
42 W. Yu, H. Zhou, B. Q. Li and S. Ding, *ACS Appl. Mater. Interfaces*, 2017, **9**, 4597–4604.
43 W. Li, Y. Li, M. Su, B. An, J. Liu, D. Su, L. Li, F. Li and Y. Song, *J. Mater. Chem. A*, 2017, **5**, 16281–16288.
44 Y. Liu, B. Zhang, Q. Xu, Y. Hou, S. Seyedin, S. Qin, G. G. Wallace, S. Beirne, J. M. Razal and J. Chen, *Adv. Funct. Mater.*, 2018, **28**, 1706592.
45 K. Shen, J. Ding and S. Yang, *Adv. Energy Mater.*, 2018, **8**, 1800408.
46 Y. Zhang, B. Wang, F. Liu, J. Cheng, X.-w. Zhang and L. Zhang, *Nano Energy*, 2016, **27**, 627–637.
47 T. Wang, Y. Guo, B. Zhao, S. Yu, H.-P. Yang, D. Lu, X.-Z. Fu, R. Sun and C.-P. Wong, *J. Power Sources*, 2015, **286**, 371–379.
48 W. Liu, X. Yan, J. Chen, Y. Feng and Q. Xue, *Nanoscale*, 2013, **5**, 6053–6062.
49 B. Zheng, T. Huang, L. Kou, X. Zhao, K. Gopalsamy and C. Gao, *J. Mater. Chem. A*, 2014, **2**, 9736–9743.

